**Proceedings of the ASME 2013 Fluids Engineering Division Summer Meeting**
**FEDSM2013**
**July 7-11, 2013, Incline Village, Nevada, USA**

# FEDSM2013-16481

# TOWARD WALL MODELING IN CARTESIAN GRID SOLVER USING OVERSET GRID TECHNIQUE FOR SHIP HYDRODYNAMICS

**Akira Hanaoka**
IIHR - Hydroscience & Engineering, University of Iowa
Iowa City, Iowa, USA

**Jianming Yang**
IIHR - Hydroscience & Engineering, University of Iowa
Iowa City, Iowa, USA

**Frederick Stern**
IIHR - Hydroscience & Engineering, University of Iowa
Iowa City, Iowa, USA

## ABSTRACT

A Cartesian grid solver is coupled with an orthogonal curvilinear grid solver using overset grid interpolation and a coupled pressure Poisson solver. It aims at resolving the boundary layer on the body surface effectively. SUGGAR code, an overset grid assembly program, provides overset grid information of a Cartesian background grid and a thin orthogonal body-fitted grid to resolve the boundary layer on the surface. The overset grid information is used to interpolate velocity, pressure, turbulence quantities, and level set function. A coupled pressure Poisson equation is solved using PETSc. The coupled curvilinear/Cartesian grid solver has been applied to two-phase turbulent flows past a circular cylinder and has shown good agreement with the experimental data and the LES results in the literature. The solver is being applied to a free surface flow around Wigley's parabolic hull form at Re = $3.4\times10^6$ and Fr = 0.25. The numerical results are promising compared to an experimental result of wave elevations at the same Fr.

## MOTIVATION AND OBJECTIVE

Computational fluid dynamics (CFD) solvers with high fidelity are required to perform accurate simulations of turbulent flows. Such CFD solvers should include high-order numerical schemes, accurate turbulence modeling, and good scalability of high performance computing (HPC). Simplicity of generating computational grids is also important for complex geometries such as those observed in ship hydrodynamics. Generation of a body-fitted structured grid around the complex geometry surface is difficult, and mesh quality, namely mesh orthogonality and mesh smoothness, often becomes an issue. On the other hand, unstructured grids show greater flexibility to geometry shapes and are easier to generate around the complex surfaces than the structured grids. However, implementation of high-order numerical schemes and accurate turbulence models such as large eddy simulation (LES) is difficult to the unstructured grid solvers. CFD solvers using a Cartesian grid with an immersed boundary method (IBM) involve extremely easy grid generation and allow implementation of high-order numerical schemes easily. Also, HPC scalability of the Cartesian grid solvers is better than that of the curvilinear structured grid solvers. Because of these features, the Cartesian grid solvers with IBM are well suited for accurate numerical simulations of turbulent flows, such as LES (Yang and Stern, 2009). However, the Cartesian grid solvers require very large grids to adequately resolve boundary layers at high Reynolds numbers. Adaptive local grid refinement near the solid wall can lead to reduction of the grid size (Iaccarino et al., 2004), but still the near-wall grid resolution is very expensive. Moreover, the fine near-wall resolutions require very small time steps to simulate unsteady or developing flows accurately. Thus, wall layer (WL) modeling is an important issue for the Cartesian grid solvers to achieve appropriate resolution of the viscous flows around the solid surfaces.

A WL modeling approach proposed by Yang and Stern (2009) is a coupled curvilinear/Cartesian grid method. In this method, curvilinear structured grids are used to resolve the boundary layers on the solid surfaces and Cartesian grids to compute the flow regions out of the boundary layers. Different CFD solvers are applied to the body-fitted curvilinear grids and the Cartesian background grids. Those solvers can be coupled using an overset grid method.

The Structured, Unstructured, and Generalized overset Grid AssembleR (SUGGAR) code was developed as an overset grid assembly program by Noack (2005). The SUGGAR code can create a single composite grid from multiple overlapping structured, unstructured, and/or general polyhedral grids for both node-centered and cell-centered flow solvers. It has been incorporated into existing flow solvers, and the solvers with the overset grid capability have been validated for several problems including static or dynamic objects (Pandya et al., 2005;

Carrica et al., 2007; Mulvihill and Yang, 2007; Koomullil et al., 2008).

The objective of this study is development of a new wall layer model for a Cartesian grid CFD solver. In the wall layer modeling, a thin structured WL grid and a non-uniform Cartesian grid are used to resolve the boundary layer on a solid surface and the flow region away from the surface, respectively. The WL grid is so thin that the grid orthogonality is maintained everywhere inside the grid. The Cartesian background grid part is solved by a Cartesian grid CFD solver, which is called CFDShip-Iowa version 6 (V6-IBM hereafter) developed on the basis of an immersed boundary method for ship hydrodynamics. Another CFD solver requiring a body-fitted orthogonal curvilinear grid is applied into the WL grid. This solver is named CFDShip-Iowa version 6.2 (V6-OC hereafter) and has been developed from V6-IBM by Suh et al. (2011). Therefore V6-OC has the similar architecture to that of V6-IBM. An overset grid method is used to couple V6-IBM and V6-OC. In the overset grid method, all the flow variables are interpolated from one grid block to another through the interface between the WL grid and the Cartesian background grid. SUGGAR code writes the grid connectivity information into a file that identifies grid points necessary for the overset grid interpolation. In order to satisfy mass conservation across the overlapping part, a pressure Poisson equation is solved in a strongly coupled manner using the PETSc toolkit (Balay et al., 2012). In this strongly coupled manner, the pressure Poisson equations and the overset interpolation equations are encompassed from both V6-IBM and V6-OC and solved together by an iterative method. The application of V6-OC into V6-IBM as the wall layer model has led to development of a coupled orthogonal curvilinear/Cartesian grid solver named CFDShip-Iowa version 6.2.5 (V6.2.5 hereafter).

## COMPUTATIONAL METHODS

### Mathematical models

Both V6-IBM and V6-OC solve the unsteady, three-dimensional, incompressible Navier-Stokes equations:

$$\frac{\partial \boldsymbol{u}}{\partial t} + \boldsymbol{u}\cdot\nabla\boldsymbol{u} = \frac{1}{\rho}\nabla\cdot(-p\boldsymbol{I} + \boldsymbol{T}) + \boldsymbol{g} \tag{1}$$

$$\nabla\cdot\boldsymbol{u} = 0 \tag{2}$$

where

$$\boldsymbol{T} = 2\mu\boldsymbol{S} \tag{3}$$

and

$$\boldsymbol{S} = \frac{1}{2}[\nabla\boldsymbol{u} + (\nabla\boldsymbol{u})^T] \tag{4}$$

Interfaces between two immiscible fluids are defined as the zero level set of a signed distance function or the level-set function which is advanced by its evolution equation:

$$\frac{\partial\phi}{\partial t} + (\boldsymbol{u}\cdot\nabla)\phi = 0 \tag{5}$$

The reinitialization equation is iteratively solved to keep the level-set function as a signed distance function in the course of its evolution:

$$\frac{\partial\phi}{\partial\tau} + S(\phi_0)(|\nabla\phi| - 1) = 0 \tag{6}$$

where

$$S(\phi_0) = \frac{\phi_0}{\sqrt{{\phi_0}^2 + (\Delta h)^2}} \tag{7}$$

Each phase of constant density and viscosity is defined by the level-set function in the computational domain. At the phase interface, the density keeps its sharp jump, whereas the viscosity is smoothed over a transition band across the interface.

V6.2.5 implements a large eddy simulation (LES) method, so the Navier-Stokes equations are spatially filtered such that the large, energy-carrying eddies are resolved while the small-scale, dissipative eddies are modeled by a subgrid-scale (SGS) model. The Smagorinsky model is used to model the SGS stress tensor in the Navier-Stokes equations. The model parameter is determined as C = 0.03. The Van Driest damping function (1956) is adopted to ensure the proper asymptotic behavior for the SGS stresses in the thin WL grid around the body. Therefore, the turbulent eddy viscosity in the WL grid is calculated as

$$\nu_t = C\Delta^2|\bar{\boldsymbol{S}}|\left(1 - \exp\left(\frac{-r^+}{25}\right)\right)^2 \tag{8}$$

### Numerical methods

A finite difference method is used to discretize the Navier-Stokes equations on non-uniform staggered grids in which the velocity components are defined at centers of cell faces and all other variables are defined at cell centers.

A four-step fractional-step method is employed for velocity-pressure coupling, in which a pressure Poisson equation is solved to enforce the continuity equation. For time advancement, a second-order semi-implicit scheme is adopted to integrate the momentum equations with the second-order Crank-Nicolson scheme for the diagonal viscous terms and the second-order Adams-Bashforth scheme for the other viscous terms and the convection terms. The processes in the four-step fractional-step method are as follows:

1. Predictor

$$\frac{\hat{u}_i - u_i^n}{\Delta t} = \frac{1}{2}(3A_i^n - A_i^{n-1}) + \frac{1}{2}(C_i^{n+1} + C_i^n) - Grad_i(p^n) \tag{9}$$

2. First corrector

$$\frac{u_i^* - \hat{u}_i}{\Delta t} = Grad_i(p^n) \tag{10}$$

3. Pressure Poisson equation

$$\frac{\partial}{\partial x_i} Grad_i(p^{n+1}) = \frac{1}{\Delta t} \frac{\partial u_i^*}{\partial x_i} \tag{11}$$

4. Second corrector

$$\frac{u_i^{n+1} - u_i^*}{\Delta t} = -Grad_i(p^{n+1}) \tag{12}$$

To solve Eq. (9), the diffusion and convective terms are discretized by the standard second-order central difference scheme and a fifth-order HJ-WENO scheme, respectively. The gravity terms do not appear in Eq. (9) explicitly since they are incorporated into the pressure gradient term $Grad_i(p)$ through the jump condition across the interface. The details can be referred to in Yang and Stern (2009).

The level-set evolution and reinitialization equations are solved using third-order TVD Runge-Kutta scheme for the time advancement and fifth-order HJ-WENO scheme for the spatial discretization. The local (narrow band) level-set method is used to identify a narrow band of several grid cell widths around the zero level set at each time step, where the level set evolution and reinitialization equations are solved. Again, the details can be referred to in Yang and Stern (2009).

Figure 1 (a) shows a WL grid overlapping with a Cartesian background grid for V6.2.5 simulation of flow past a circular cylinder. As shown in Figure 1 (a), the whole WL grids are included inside the Cartesian background grids for all the V6.2.5 simulations. The grid connectivity information is obtained by three overset grid assembly processes performed by the SUGGAR code, an overset grid assembly program originally designed for moving body simulations. At the beginning of the processes, the SUGGAR code identifies hole points within the grids, which are excluded from the numerical computations. In Figure 1 (b), the Cartesian grid points highlighted by green become the hole points because they are inside the WL grid or the circular cylinder. The next step in the overset grid assembly process is identification of fringe points which receive flow variables interpolated from other grids. Once all the fringe points are specified, the final step searches donor points which interpolate the flow variables to the corresponding fringe points and identifies the interpolation weights of the donor points. Figure 1 (b) and (c) show the fringe points (blue) and active points (red) on which the governing equations are solved. The fringe points provide the Dirichlet boundary conditions that V6-IBM and V6-OC in V6.2.5 use. The details of the overset grid assembly process in the SUGGAR code are described in Noack (2005).

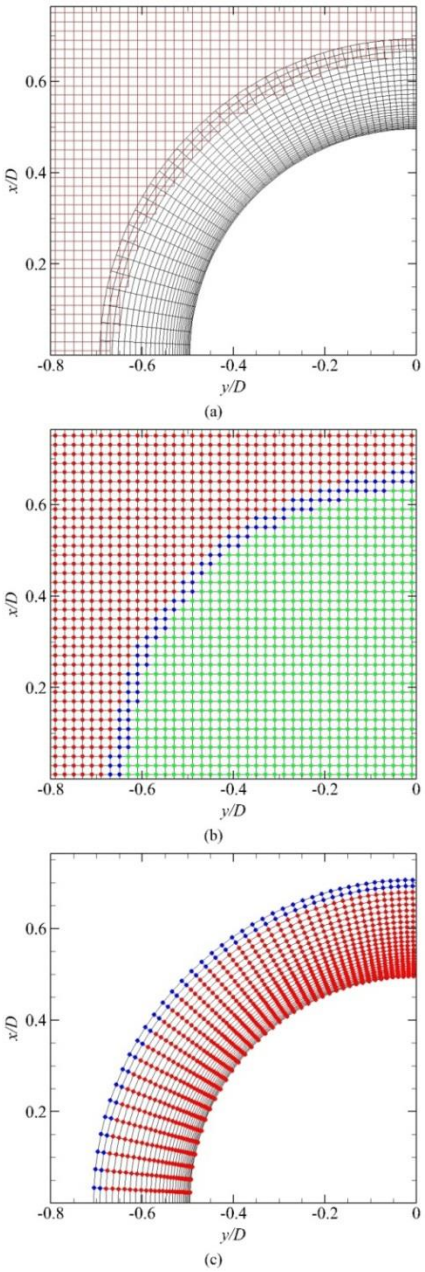


**Figure 1 (a) Overset grid configuration for flow past a circular cylinder; (b) active points (red), fringe points (blue), and hole points (green) in the Cartesian background grid; (c) active points (red) and fringe points (blue) in the wall layer grid**

Figure 2 shows the overall solution strategy in V6.2.5. Since the current study handles only flow problems with static bodies, it is sufficient that the SUGGAR code is executed before the numerical simulations. The grid connectivity information specifies which grid point is the hole, fringe, or active point, and what the interpolation weights of the donors are, as described above. The grid connectivity information is written in a file which V6.2.5 reads together with the input data

necessary for the simulation. Since both V6-IBM and V6-OC perform the domain decompositions using the MPI library, V6.2.5 splits all the processors into the component solvers which are executed simultaneously. Since both of the solvers have the same numerical methods, the overset interpolation can be performed in a straightforward manner; each flow variable is interpolated after it is solved by the governing equations. For the velocity components, the interpolation is also done for the intermediate velocities in the predictor step and the first corrector step of the four-step fractional-step method to obtain the smooth velocity distribution across the overlapping part of the grid blocks.

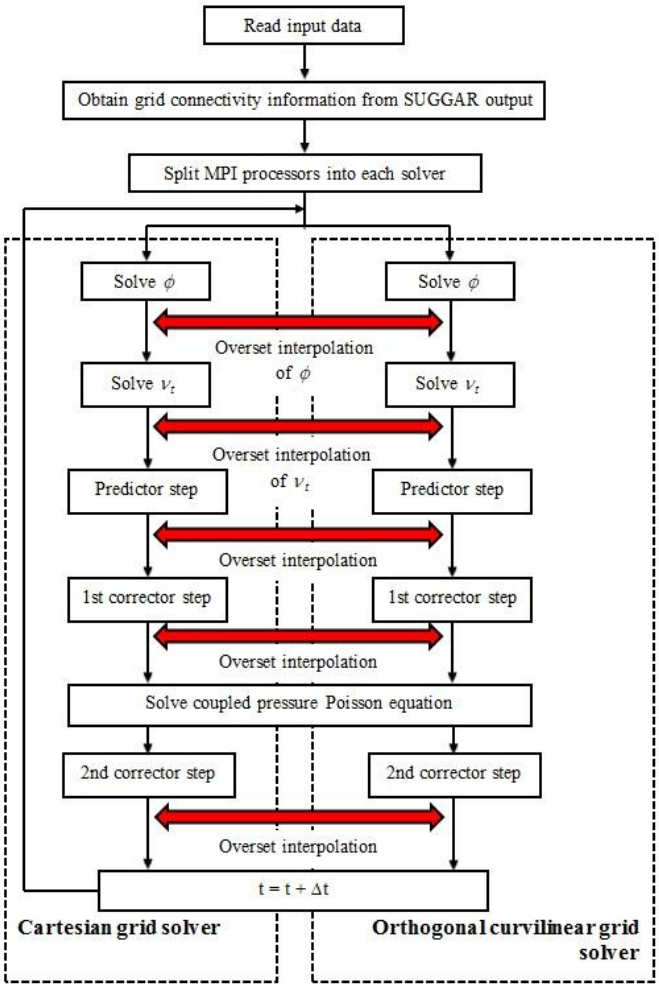


**Figure 2 Solution strategy of coupled orthogonal curvilinear/Cartesian grid solver**

The overset interpolation in V6.2.5 is performed for the variables at the centers of the cells. Therefore, the velocity components at the cell centers need to be calculated from those at the centers of the cell faces which are solved by the momentum equations. Moreover, V6-OC incorporated in V6.2.5 as the curvilinear grid solver computes the contravariant velocity components along the curvilinear coordinate system. Those contravariant velocity components have to be transformed into those in the Cartesian coordinate system before the overset interpolation. The contravariant velocity components at the cell centers are obtained by the arithmetic mean. Then, the velocity components can be transformed into those along the Cartesian coordinates as Eq. (13). After the overset interpolation, the Cartesian velocity components at the cell centers are transformed into the contravariant velocity components as Eq. (14).

$$\begin{pmatrix} U \\ V \\ W \end{pmatrix} \equiv \begin{bmatrix} \frac{\partial x}{\partial \xi} & \frac{\partial x}{\partial \eta} & \frac{\partial x}{\partial \zeta} \\ \frac{\partial y}{\partial \xi} & \frac{\partial y}{\partial \eta} & \frac{\partial y}{\partial \zeta} \\ \frac{\partial z}{\partial \xi} & \frac{\partial z}{\partial \eta} & \frac{\partial z}{\partial \zeta} \end{bmatrix} \begin{pmatrix} u \\ v \\ w \end{pmatrix} \tag{13}$$

$$\begin{pmatrix} u \\ v \\ w \end{pmatrix} \equiv \begin{bmatrix} \frac{\partial \xi}{\partial x} & \frac{\partial \xi}{\partial y} & \frac{\partial \xi}{\partial z} \\ \frac{\partial \eta}{\partial x} & \frac{\partial \eta}{\partial y} & \frac{\partial \eta}{\partial z} \\ \frac{\partial \zeta}{\partial x} & \frac{\partial \zeta}{\partial y} & \frac{\partial \zeta}{\partial z} \end{bmatrix} \begin{pmatrix} U \\ V \\ W \end{pmatrix} \tag{14}$$

A pressure Poisson equation is solved in a strongly coupled manner using the PETSc toolkit (Balay et al., 2012). In this strong coupling of the pressure Poisson equation, the pressure Poisson equations and the overset interpolation equations are encompassed from both V6-IBM and V6-OC and solved together by Krylov subspace based GMRES iterative method with ASM preconditioner. Therefore, both the continuity equation and the overset interpolation relation are satisfied in both of the CFD solvers. In the coupled pressure Poisson equation, the left hand side (LHS) matrix consists of 1-point stencils for the hole points, 9-point stencils for the fringe points, 7-point stencils for the active points shown in Figure 1. The LHS matrix is assembled only at the first time step as the grids are static, whereas the right hand side (RHS) vector is updated at every time step.

## NUMERICAL SIMULATIONS OF TWO-PHASE FLOWS PAST A CIRCULAR CYLINDER

A flow past a circular cylinder is an ideal case to validate V6.2.5 because it involves an orthogonal curvilinear WL grid based on cylindrical coordinate system. Since the flows past free surface piercing circular cylinders have received much less attention than the single-phase flows, only a few experimental and numerical studies on the two-phase flows around the circular cylinders are available in the literature. In spite of this, the two-phase flows past the circular cylinders still play important roles in various engineering applications including offshore structures and surface vessels. Moreover, the flows past the free surface piercing circular cylinders include

complicated phenomena due to the generation of waves in various forms, the interactions of the waves with the body and vortices, the interfacial effects like bubble entrainment and surface tension, and three-dimensional flow separation, which are of great interest in fluid mechanics. Thus, the viability and accuracy of the WL modeling in V6.2.5 are investigated by considering the two-phase turbulent flows past circular cylinders.

**Table 1 Simulation conditions for turbulent flows past circular cylinders**

| Cases | Fr | Re | Grid resolution | |
|---|---|---|---|---|
| | | | $N_x \times N_y \times N_z$ | $N_r \times N_\theta \times N_z$ |
| 2.7E4-0.20 | 0.20 | $2.70\times10^4$ | 264×240×128 | 24×128×128 |
| 2.7E4-0.80 | 0.80 | $2.70\times10^4$ | | |
| 4.58E5-1.64 | 1.64 | $4.58\times10^5$ | 336×328×300 | 28×256×300 |

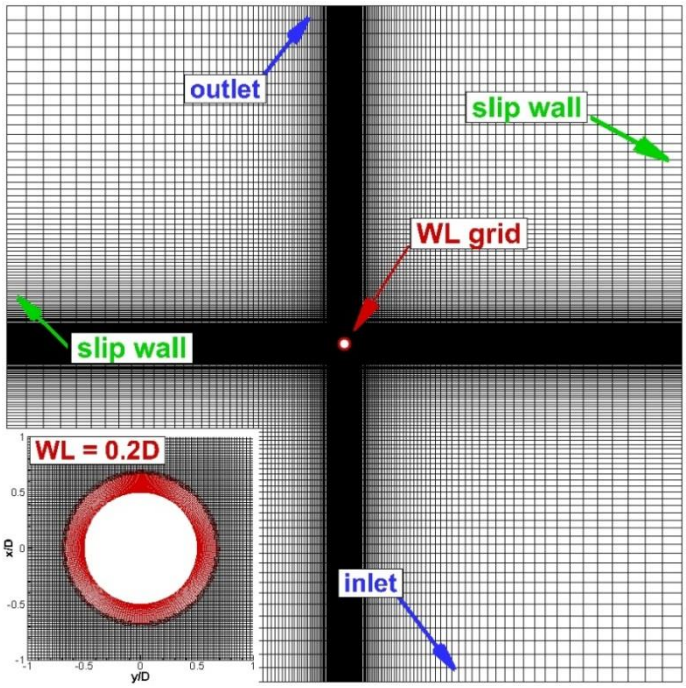


**Figure 3 Computational grids and boundary conditions for V6.2.5, inset shows the WL domain size of 0.2D.**

For the two-phase flows, Hay (1947) measured the maximum heights of the bow waves in front of the circular cylinder and the depths of the depression on the center line behind the cylinder. Chaplin and Teigen (2003) review the experimental study of Hay (1947) and also show their own measurement of the drag coefficients ($C_D$) as a function of Fr with a constant ratio Re/Fr = $2.79\times10^5$. Inoue et al. (1993) conducted an experiment of the free surface flow past a circular cylinder at Re = $2.7\times10^4$ and Fr = 0.8. They measured the mean free surface elevations and the root mean square (RMS) of the elevation fluctuations around the circular cylinder. Profiles of the streamwise velocity and the free surface elevation are also available from the study. Kawamura et al. (2002) investigated the flows around a free surface piercing circular cylinder at Re = $2.7\times10^4$ with three different Froude numbers Fr = 0.2, 0.5, and 0.8. Yu et al. (2008) studied free surface flows past a circular cylinder at Fr up to 3.0 and Re up to $1.0\times10^5$. Suh et al. (2011) performed LES of the flows past a free surface piercing circular cylinder at Fr = 0.2 and 0.8 with the same Reynolds number Re = $2.7\times10^4$ using V6-OC. Koo (2011) extended the study of Suh et al. (2011) and used V6-OC to perform numerical simulations with conditions mainly based on the experiments of Chaplin and Teigen (2003). Those numerical studies show the detailed results of the free surfaces, the mean flow and turbulence statistics, the vortical structures, and the hydrodynamic forces at several Reynolds numbers up to Re = $4.58\times10^5$ and Froude numbers up to Fr = 1.64.

**Table 2 Drag coefficients and RMS of lift fluctuations of two-phase turbulent flows**

| Case | Fr | Re | $C_D$ | $C_L^{RMS}$ | $y^+$ |
|---|---|---|---|---|---|
| Experiment | | $2.7\times10^4$ | 1.200 | 0.450 | - |
| Kawamura et al. (2002) **(E)** | 0.20 | | 1.120 **(-6.7%)** | 0.320 **(-29%)** | - |
| 2.7E4-0.20 **(E)** | | | 1.104 **(-8.0%)** | 0.324 **(-28%)** | 0.968 |
| Kawamura et al. (2002) **(E)** | 0.80 | | 0.970 **(-19%)** | 0.240 **(-47%)** | - |
| Suh et al. (2011) **(E)** | | | 0.984 **(-18%)** | 0.220 **(-51%)** | 0.485 |
| 2.7E4-0.80 **(E)** | | | 0.985 **(-18%)** | 0.219 **(-51%)** | 0.969 |
| Experiment | 1.64 | $4.58\times10^5$ | 0.635 | - | - |
| Koo (2011) **(E)** | | | 0.560 **(13%)** | - | 0.960 |
| 4.58E5-1.64 **(E)** | | | 0.623 **(-1.9%)** | - | 0.954 |

Table 1 summarizes the simulation conditions for the turbulent flows past circular cylinders. For the two-phase flows at Fr = 0.2 and 0.8 (2.7E4-0.20 and 2.7E4-0.80), the Cartesian domain size is $-10 \le x/D \le 15$, $-10 \le y/D \le 10$ and $-4 \le z/D \le 2$, and the grid consists of 8.5M points. For the Fr = 1.64 case, the domain size is $-15 \le x/D \le 45$, $-20 \le y/D \le 20$ and $-4 \le z/D \le 2$, and the grid consists of 35M points.

Figure 3 shows X-Y horizontal planes of the grid domains and the boundary conditions used by V6.2.5 for the circular cylinder cases. The Cartesian background grid is used to specify the inlet, outlet, and slip wall boundary conditions. The slip wall boundary condition specifies zero velocity in the normal direction to the face and the Neumann condition for the other directions. The WL grid is used to specify the no-slip boundary conditions on the wall surface. The Cartesian grid and WL grid solvers communicate with each other via the overset boundary condition at J-MAX plane of the WL grid.

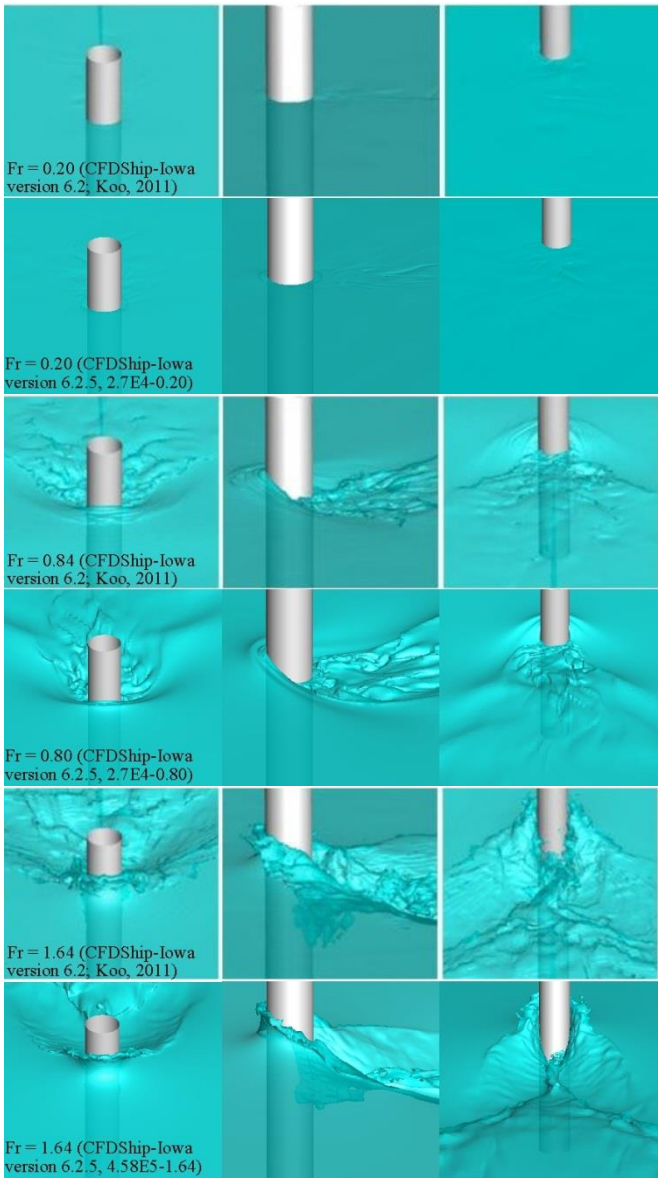


**Figure 4 Instantaneous free surfaces around the circular cylinder**

Table 2 compares the mean $C_D$ and the RMS of the lift coefficients ($C_L^{RMS}$). Unfortunately, no experimental data are available about the hydrodynamic forces of the circular cylinder in the two-phase flows at Fr = 0.2 and 0.8 with Re = $2.7\times10^4$. However, the experimental measurement of the single-phase flow at the same Re can be obtained from Szepessy and Bearman (1992). The experimental data at Re = $4.58\times10^5$ and Fr = 1.64 was taken from Chaplin and Teigen (2003). The predictions of 2.7E4-0.20 and 2.7E4-0.80 show up to 18% lower $C_D$ and up to 51% lower $C_L^{RMS}$ than the experimental data of the single-phase flow at the same Re (Szepessy and Bearman, 1992). The effects of the deformation of the free surface probably result in the lower values of $C_D$ and $C_L^{RMS}$ (Kawamura et al., 2002; Yu et al., 2008). It is noted that the V6.2.5 predictions approach the experimental data as Fr decreases. This trend is consistent with that observed in Kawamura et al. (2002), and the predictions of both 2.7E4-0.20 and 2.7E4-0.80 compare within 4% of the LES results of Kawamura et al. (2002) and Suh et al. (2011). Good agreement was obtained between the experimental data of Chaplin and Teigen (2003) and the prediction of 4.58E5-1.64, whose difference is about 2%.

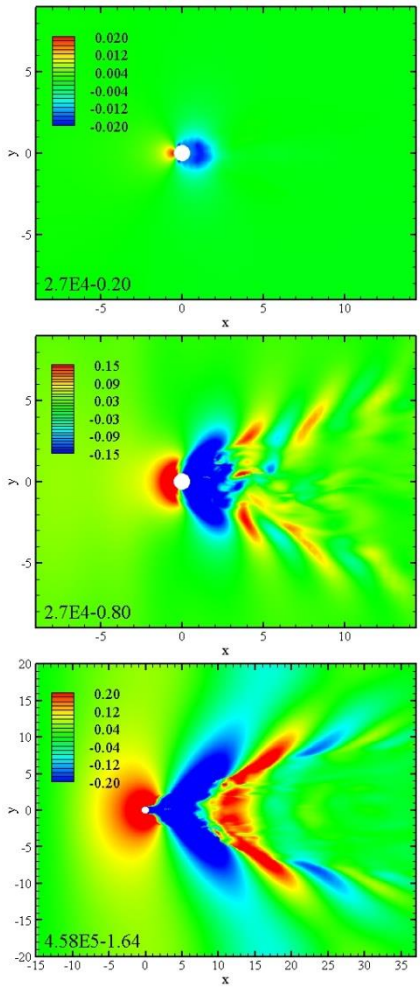


**Figure 5 Instantaneous free surfaces in the wake behind the circular cylinder**

Figures 4 and 5 show the instantaneous free surfaces computed by 2.7E4-0.20, 2.7E4-0.80, and 4.58E5-1.64. In Figure 4, the numerical results of V6.2.5 show the similar characteristics to those predicted by V6-OC (Koo, 2011). At Fr = 0.20, the deformation of the free surface is negligibly small and no waves are generated in the wake behind the cylinder. On the other hand, the free surfaces are deformed largely at higher Fr = 0.80 and 1.64. Bow waves are generated in front of the cylinder. The depressions exist on the downstream side of the cylinder. The free surfaces are very rough around the cylinder, and this indicates the existence of vortical structures below the free surface (Suh et al., 2011). Figure 5 clearly shows Kelvin waves generated in the wake at Fr = 0.80 and 1.64. The wave

lengths predicted by V6.2.5 at both Fr are close to the theoretical values, i.e., $2\pi Fr^2$.

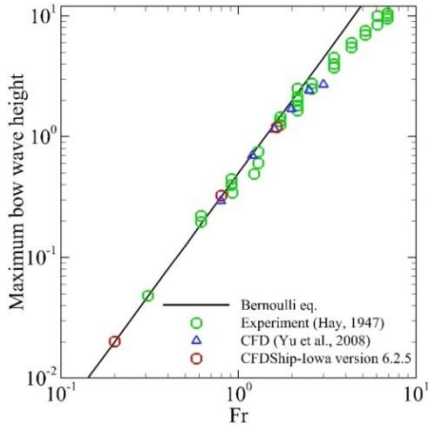


**Figure 6 Maximum heights of bow waves compared with the line of Bernoulli equation**

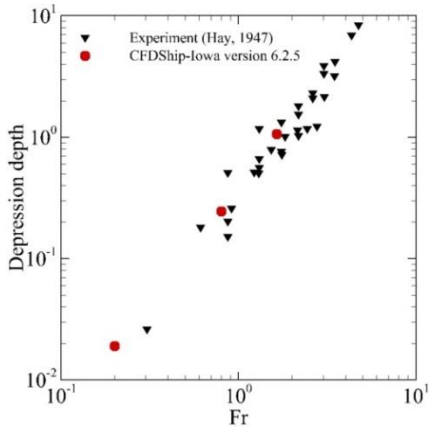


**Figure 7 Depths of depressions behind the cylinder on the center plane of the wake**

Some features of the mean free surfaces are compared qualitatively and quantitatively. Figures 6 and 7 compare the maximum heights of the bow waves and the depths of the depressions on the center plane of the wake, respectively. The experimental data was obtained from Hay (1947) reviewed in Chaplin and Teigen (2003). The solid line shows Bernoulli equation result and indicates possible maximum bow wave heights ($=Fr^2/2$). The bow wave heights and depression depths predicted by V6.2.5 are in fairly good agreement with the experimental data and the Bernoulli equation result.

Figure 8 compares the near wake profiles of the mean free surface elevations ($h_{mean}$) and the RMS of the free surface fluctuations ($h_{rms}$) between the experimental data (Inoue et al, 1993), the LES results in the literature (Kawamura et al., 2002; Suh et al., 2011; Koo, 2011), and V6.2.5 (2.7E4-0.20, 2.7E4-0.80, and 4.58E5-1.64). V6.2.5 predicts both mean interface elevations and interface fluctuations at Fr = 0.20 in good agreement with the CFD results of Kawamura et al. (2002). Note that the differences between the numerical results are small compared to those observed at higher Fr. Although the numerical results of 2.7E4-0.80 agree well with the experimental data of Inoue et al. (1993), V6.2.5 under-predicts the depression on the profile at x = 0.9 near the center plane of the wake. The prediction is more similar to the V6-OC result by Suh et al. (2011). The results of 4.58E5-1.64 are in good agreement with those of the V6-OC by Koo (2011).

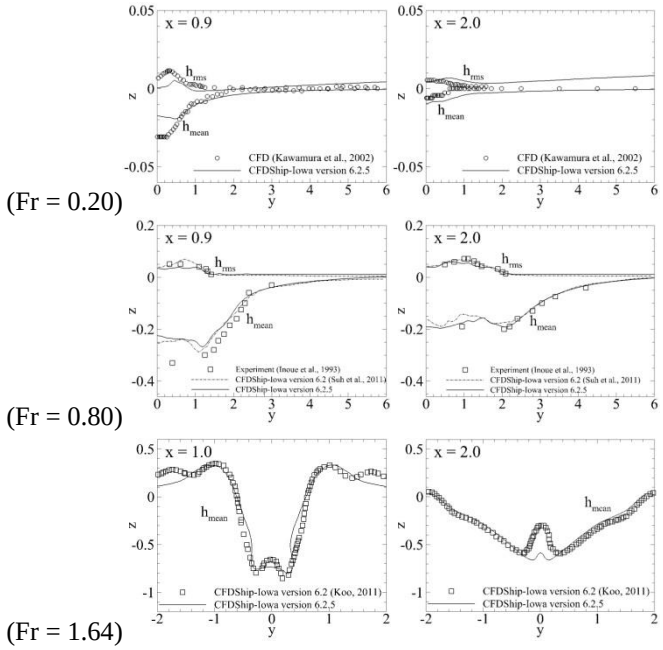


**Figure 8 Transverse profiles of the mean free surface elevations near the cylinder**

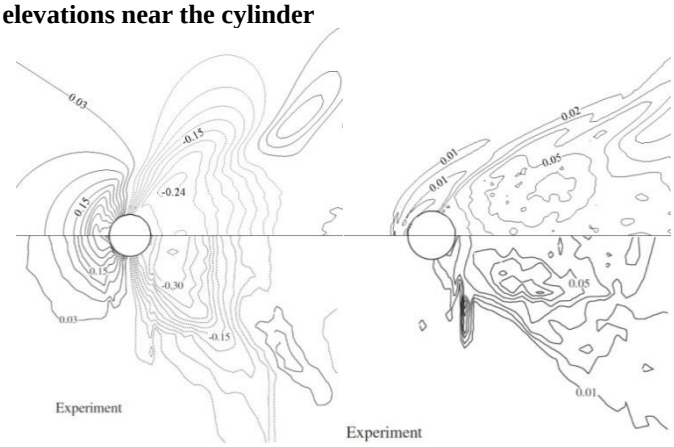


**Figure 9 Mean free surface around the cylinder at Re = $2.7\times10^4$ and Fr = 0.80: (left panel) elevations; (right panel) RMS of the free surface fluctuations**

Inoue et al. (1993) shows the detailed measurement of the free surface elevations and the RMS of the free surface fluctuations around the circular cylinder at Re = $2.7\times10^4$ and Fr = 0.80. The experimental data are compared with the numerical results of 2.7E4-0.80 in Figure 9. V6.2.5 captures all the features in the experimental data well, i.e., the bow wave on the upstream side of the cylinder, an almost constant slope leading

to the large depression on the downstream side, and the Kelvin waves diverging into the wake. The V6.2.5 result of the free surface fluctuations shows good agreement with the experimental data with regard to the overall distribution and the location of the peak value. The peak value is slightly under-predicted than the experimental data. V6.2.5 predicts fluctuations on the front side of the cylinder. This trend is similar to the V6-OC result in Suh et al. (2011), and it is explained that the front fluctuations are due to the presence of the necklace vortices.

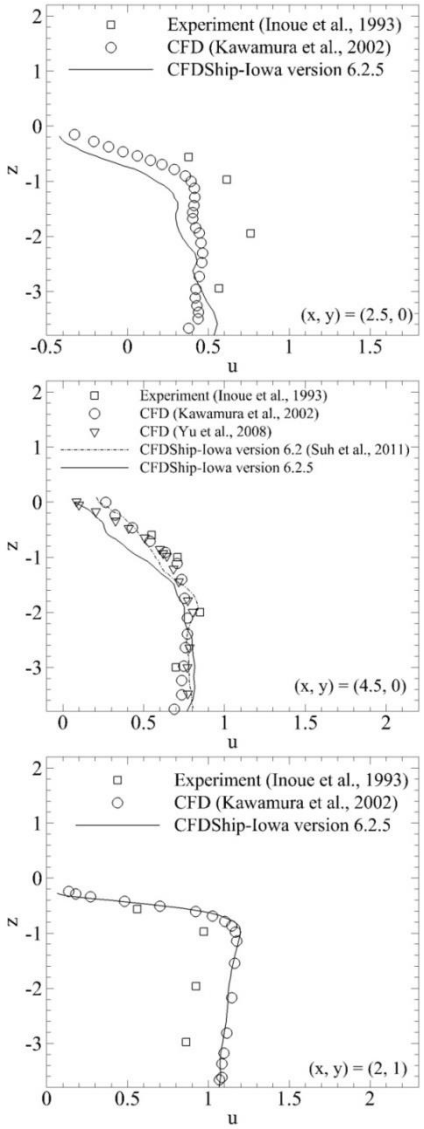


**Figure 10 Vertical profiles of the mean streamwise velocity at Re = $2.7\times10^4$ and Fr = 0.80**

Inoue et al. (1993) also measured the vertical profiles of the mean streamwise velocity in the wake at Re = $2.70\times10^4$ and Fr = 0.80. The profiles are compared in Figure 10. The experimental data of Inoue et al. (1993) shows that the streamwise velocity is almost constant in the deep flow and decreases as the free surface is approached. This trend corresponds to the recirculation region on the free surface, which is longer in the streamwise direction and wider in the transverse direction than that in the deep flow (Suh et al., 2011). The results of 2.7E4-0.80 capture the above features of the streamwise velocity and show fair agreement with the experimental data and the LES results of Kawamura et al. (2002), Yu et al. (2008), and Suh et al (2011).

Pressure distributions on the cylinder surface in the deep flow are compared with the experimental data of the single-phase flows at similar Re in Figure 11. The experimental data at subcritical Re = $2\times10^4$ was obtained from Norberg (1992), whereas the data of Flachsbart at supercritical Re = $6.7\times10^5$ was obtained from Zdravkovich (1997). The experimental data at the subcritical Re shows decreasing pressure in the separated region after the separation point, while the pressure at the supercritical Re is almost constant in the separated region. The separation point moves downstream at the supercritical Re compared to the subcritical Re, which indicates the delayed separation at the higher supercritical Re. In addition, the experimental data at Re = $6.7\times10^5$ contains a kink near 110°, indicating the presence of a separation bubble which is difficult to reproduce (Catalano et al; 2003). All of the V6.2.5 predictions in the deep flows are in excellent agreement with the experimental data at similar Re.

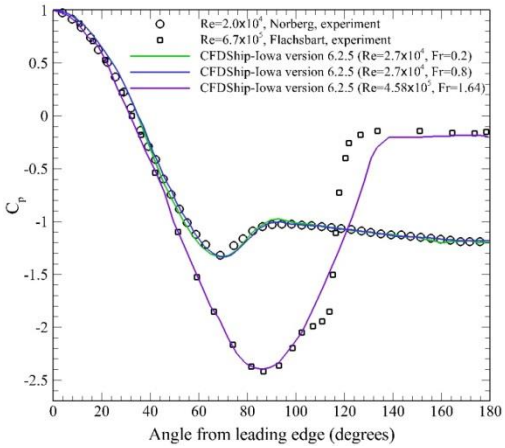


**Figure 11 Pressure distributions on the cylinder surface in the deep flow region**

## NUMERICAL SIMULATION OF A FREE SURFACE FLOW PAST WIGLEY HULL

The Wigley hull is a mathematical representation of an actual ship hull and is defined as

$$y = \frac{1}{2}B\left\{1-\left(\frac{2x}{L}\right)^2\right\}\left\{1-\left(\frac{z}{T}\right)^2\right\}, \quad z \le 0 \qquad (15)$$

The geometry of the hull above z = 0 was obtained by extruding the section at that plane along the vertical direction. Figure 12 shows different views of the Wigley hull. Because of

the simple geometry shape, the WL grid for the V6.2.5 simulation can be orthogonal around the hull surface.

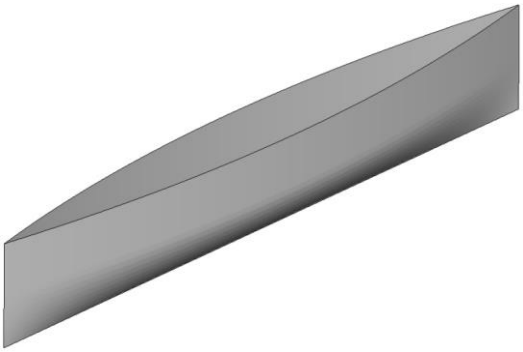

**Figure 12 Wigley hull geometry**

Table 3 summarizes the simulation conditions for the free surface flow past Wigley hull. The Cartesian domain size is -1 $\leq$ x/L $\leq$ 1, 0 $\leq$ y/L $\leq$ 1 and -0.5 $\leq$ z/D $\leq$ 0.06, and the grid consists of 18.8M points.

**Table 3 Simulation conditions for the free surface flow past Wigley hull**

| Fr | Re | Grid resolution | |
|---|---|---|---|
| | | $N_x \times N_y \times N_z$ | $N_r \times N_\theta \times N_z$ |
| 0.25 | $3.4 \times 10^6$ | 515×214×162 | 21×282×162 |

Figure 13 clearly shows Kelvin waves around Wigley hull. The wave elevations are compared with the experimental data of Inui and Kajitani (1968) in Figure 14. Although the simulation is still in progress, the numerical result of V6.2.5 shows diverging Kelvin waves similar to those in the experimental data.

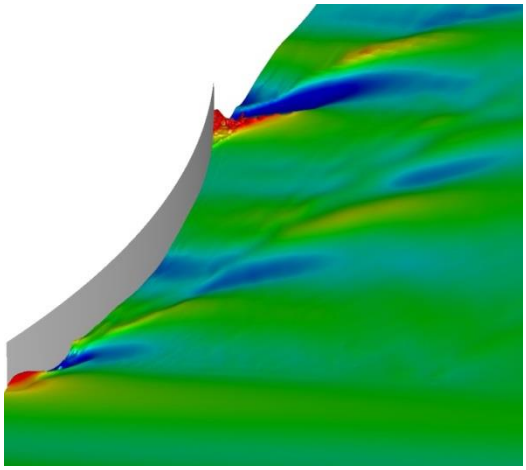

**Figure 13 Wave elevations around Wigley hull**

## CONCLUSION

A Cartesian grid CFD solver has been coupled with an orthogonal curvilinear grid solver. The purpose of the coupling is to achieve appropriate resolution of the boundary layers. The SUGGAR code provides the grid connectivity information to interpolate the flow variables from one solver to another. A coupled pressure Poisson equation is solved using PETSc in order to satisfy both mass conservation and overset interpolation relation in both of the CFD solvers.

The coupled curvilinear/Cartesian grid solver developed as V6.2.5 in this study has been validated for two-phase turbulent flows past a circular cylinder. The numerical results of V6.2.5 have shown excellent agreement with the experimental data and the LES results in the literature.

V6.2.5 was also applied to the free surface flow past Wigley hull. The numerical results are promising compared to an experimental result of wave elevations at the same Fr.

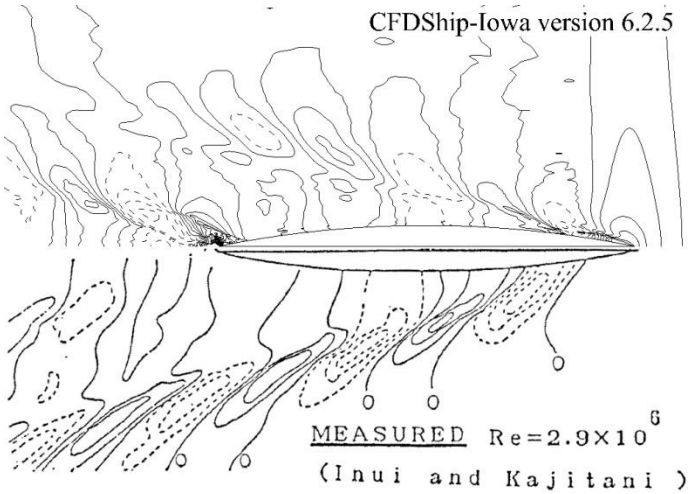


**Figure 14 Comparison of wave elevations with the experimental data. Contour interval is 0.002 and dotted lines show negative values.**

## ACKNOWLEDGMENTS

This work is sponsored by the US Office of Naval Research through research grant N000141-01-00-1-7 under the administration of Dr. Patrick Purtell.

## REFERENCES

Balay, S., Brown, J., Buschelman, K., Eijkhout, V., Gropp, W., Kaushik, D., Knepley, M., McInnes, L. C., Smith, B., and Zhang, H. 2012. "PETSc Users Manual Revision 3.3." ANL-95/11 Argonne National Laboratory.

Carrica, Pablo M., Wilson, Robert V., Noack, Ralph W., and Stern, Fred. 2007. "Ship motions using single-phase level set with dynamic overset grids." *Computer & Fluids* 36:1415-1433.

Catalano, Pietro., Wang, Meng., Iaccarino, Gianluca., and Moin, Parviz. 2003. "Numerical simulation of the flow around a circular cylinder at high Reynolds numbers." *International Journal of Heat and Fluid Flow* 24:463-469.

Chaplin, J. R., and Teigen, P. 2003. “Steady flow past a vertical surface-piercing circular cylinder.” *Journal of Fluids and Structures* 18:271-285.

Hay, A. D. 1947. “Flow about semi-submerged cylinders of finite length.” *Princeton University Report*.

Iaccarino, G., Kalitzin, G., Moin, P., and Khalighi, B. 2004. “Local Grid Refinement for an Immersed Boundary RANS Solver.” *42nd AIAA Aerospace Sciences Meeting and Exhibit* AIAA 2004-586.

Inoue, M., Baba, N., and Himeno, Y. 1993. “Experimental and numerical study of viscous flow field around an advancing vertical circular cylinder piercing a free-surface.” *Journal of Kansai Society of Naval Architecture of Japan* 220:57-64.

Inui, T., and Kajitani, H. 1968. “Bow Wave Analysis of A Simple Hull Form.” *Journal of the Society of Naval Architects of Japan* 124:19-25.

Kawamura, T., Mayer, S., Garapon, A., and Sørensen, L. 2002. “Large eddy simulation of a flow past a free surface piercing circular cylinder.” *Journal of Fluids Engineering* 124:91-101.

Koo, G. K. 2011. “Numerical study of two-phase air-water interfacial flow: Plunging wave breaking and vortex-interface interaction.” PhD diss., The University of Iowa.

Koomullil, Roy., Cheng, Gary., Soni, Bharat., Noack, Ralph., and Prewitt, Nathan. 2008. “Moving-body simulations using overset framework with rigid body dynamics.” *Mathematics and Computers in Simulation* 78:618-626.

Mulvihill, Lawrence P., and Yang, Cheng-I. 2007. “Numerical Simulation of Flow over Fully Appended ONR Body-1 with Overset Grid Scheme” *Proc. 9th International Conference on Numerical Ship Hydrodynamics*.

Noack, Ralph W. 2005. “SUGGAR: a General Capability for Moving Body Overset Grid Assembly.” *17th AIAA Computational Fluid Dynamics Conference* AIAA 2005-5117.

Norberg, C. 1992. “Pressure forces on a circular cylinder in cross flow.” *IUTAM Symposium on Bluff-Body Wakes, Dynamics and Instabilities* 275-278.

Pandya, Mohagna J., Frink, Neal T., and Noack, Ralph W. 2005. “Progress Toward Overset-Grid Moving Body Capability for USM3D Unstructured Flow Solver.” *17th AIAA Computational Fluid Dynamics Conference* AIAA 2005-5118.

Suh, Jungsoo., Yang, Jianming., and Stern, Frederick. 2001. “The effect of air-water interface on the vortex shedding from a vertical circular cylinder.” *Journal of Fluids and Structures* 27:1-22.

Szepessy, S., and Bearman, P. W. 1992. “Aspect ratio and end plate effects on vortex shedding from a circular cylinder.” *Journal of Fluids Mechanics* 234:191-217.

Van Driest, E. R. 1956. “On turbulent flow near a wall.” *Journal of the Aeronautical Sciences* 23:1007-1011.

Yang, Jianming., and Stern, Frederick. 2009. “Sharp interface immersed-boundary/level-set method for wave-body interactions.” *Journal of Computational Physics* 228:6590-6616.

Yu, G., Avital, E. J., and Williams, J. J. R. 2008. “Large eddy simulation of flow past free surface piercing circular cylinders.” *Journal of Fluids Engineering* 130:101304.1-101304.9.

Zdravkovich, M. M. 1997. “Flow Around Circular Cylinders. Fundamentals, vol. 1.” Oxford University Press.

 